Chemical Science

ROYAL SOCIETY OF CHEMISTRY

EDGE ARTICLE

View Article Online
View Journal

Cite this: DOI: 10.1039/d6sc01375a

All publication charges for this article have been paid for by the Royal Society of Chemistry

Single-atom cocatalysts engineer proton microenvironments for efficient alkaline hydrogen evolution

Guang Yang,†[ab] Minghao Yang,†[ab] Zeshuo Meng [ab] and Yi Cui *[ab]

Single-atom catalysts (SACs) are traditionally designed as the primary active sites for catalytic reactions. Here, we advance a fundamentally different conceptual framework by redefining single-atom sites as cocatalytic regulators that orchestrate reaction microenvironments rather than directly participating in catalytic turnover. Taking alkaline hydrogen evolution (HER) on Ru nanoparticles as a model reaction, we demonstrate through DFT calculations that Mo, W, and Cr single-atom cocatalysts—although intrinsically poor in hydrogen adsorption—significantly optimize the ΔG_{H^*} of neighboring Ru sites. Guided by this prediction, we synthesize Mo–Ru@CNT, which achieves near-zero overpotential at 10 mA cm^{-2}, a Tafel slope of 25.34 mV dec^{-1}, and a turnover frequency of 15.49 s^{-1} at an overpotential of 100 mV—far exceeding the performance of Ru@CNT without cocatalysts. Multi-scale characterization further revealed that the role of the single-atom cocatalyst extends beyond electronic modulation. The introduction of Mo/W/Cr single-atom sites can *in situ* generate Brønsted acidic sites during the reaction, regulating the proton concentration near the Ru sites and constructing a proton-enriched acid-like interfacial microenvironment on the Ru surface. This work redefines the functional scope of single-atom materials from active centers to cocatalytic regulators, opening a new design dimension for complex multi-step electrocatalytic reactions.

Received 16th February 2026
Accepted 4th June 2026

DOI: 10.1039/d6sc01375a

rsc.li/chemical-science

Introduction

Single-atom catalysts (SACs) have ushered in revolutionary opportunities for catalytic science due to their maximized atom utilization and unique electronic structures.[1–3] Since the concept was clearly defined in 2011, the atomically dispersed nature of SACs enables precise tuning of electronic structures and chemical properties.[4] They are frequently employed to meticulously construct active sites for a variety of catalytic reactions.[5] In the field of electrocatalysis, SACs have been extensively applied and studied in reactions such as hydrogen evolution reaction (HER),[6] oxygen reduction reaction (ORR),[7] carbon dioxide reduction reaction (CO_2RR),[8] and nitrogen reduction reaction (NRR).[9] Although SACs show broad prospects in numerous electrocatalytic reactions, their true unique value lies in providing an ideal platform at the atomic scale for understanding and regulating multi-step, complex catalytic reaction networks.[10] Particularly for reactions involving multiple intermediates that require synergistic catalysis by different functional sites, the controllability of SACs allows them to be precisely designed to target and enhance specific rate-determining steps within the reaction.[11] Therefore, the intrinsic advantages of SACs make them key to unraveling the micro-level bottlenecks of such complex reactions from an atomic perspective.

Among various catalytic reactions, the alkaline HER is a crucial half-reaction in anion exchange membrane water electrolysis (AEMWE).[12] It involves multiple steps, including the additional Volmer step for water dissociation ($H_2O + e^- \rightarrow H^*_{ad} + OH^-$) and issues such as competitive OH* adsorption. These lead to sluggish interfacial proton supply, resulting in catalyst performance that is far inferior to that in acidic HER.[13–15] In this context, modulating the hydrogen adsorption free energy (ΔG_{H^*}) of the catalyst can partially enhance the steps following water dissociation—namely, the Heyrovsky ($H_{ad}^* + H_2O + e^- \rightarrow H_2 + OH^-$) or Tafel ($H_{ad}^* + H_{ad}^* \rightarrow H_2$) steps—thereby improving the HER kinetics and overall catalyst performance.[16,17] On the other hand, introducing additional water dissociation sites and competitive adsorption sites for OH intermediates can significantly boost the overall HER kinetics originating from water dissociation, achieving a several-fold enhancement in catalyst performance. For instance, Ram Subbaraman *et al.*[18] demonstrated that by constructing a Pt–$Ni(OH)_2$ model catalyst, $Ni(OH)_2$ clusters deposited on a Pt single-crystal surface promoted water dissociation and hydrogen intermediate generation, leading to an eight-fold

[a]School of Nano Technology and Nano Bionics, University of Science and Technology of China, Hefei, 230026, China. E-mail: ycui2015@sinano.ac.cn

[b]i-lab, Vacuum Interconnected NanoTech Workstation (Nano-X), Suzhou Institute of Nano-Tech and Nano-Bionics, Chinese Academy of Sciences, Suzhou 215123, China

† These authors contributed equally.

performance improvement. Our previous work[19] also showed that constructing a Ni/NiO model catalyst, where surface NiO species facilitated the transfer of OH species from Ni metal sites to NiO, enhanced both the activity and stability of the alkaline HER catalyst. This was achieved by protecting the Ni sites from poisoning through OH adsorption. Furthermore, owing to the precise tunability of their atomic structure and coordination environment, certain single-atom materials can be introduced to enhance water adsorption/dissociation and modulate OH adsorption during alkaline HER. For example, Guo *et al.*[20] designed highly oxyphilic Cr single-atom sites connected to Pt clusters on a carbon substrate. This not only formed stable Pt–Cr covalent bonds to stabilize the Pt clusters but also, due to the high oxophilicity of the Cr sites adsorbing the OH generated from water dissociation, synergistically enhanced the water dissociation step and consequently the HER activity of the Pt sites. Similarly, Zhou *et al.*[21] found that introducing Ce single atoms to cooperate with Ru nanoparticles, leveraging the oxophilicity of Ce, facilitates coupling with hydroxyl groups post water dissociation. This avoided hydroxyl poisoning of the Ru sites, allowing better combination with hydrogen protons, and the synergy between Ce single atoms and Ru particles enhanced the alkaline HER process. These studies fully demonstrate that single-atom catalytic sites can effectively regulate specific intermediate processes in complex catalytic reactions, indirectly enhancing the overall HER performance of the material.

Building on recent advances in SAC applications and the growing understanding of proton-scarcity effects during alkaline hydrogen evolution reaction (HER), we propose a distinct conceptual framework termed single-atom cocatalysts. In this framework, atomically dispersed species contribute to catalysis through auxiliary, non-active-site pathways—an aspect that remains largely underexplored. Specifically, we focus on designing a class of catalysts composed of single-atom species from the same main group—W, Mo, and Cr—anchored on noble metal Ru nanoparticles (W/Mo/Cr single-atom–modified Ru). Unlike conventional SAC systems, in which isolated metal atoms typically serve as the primary active sites, the M–O moieties (M = W, Mo, or Cr) in our system exhibit solid-acid characteristics and dynamically regulate the interfacial proton environment during alkaline HER.[22] In this work, we therefore emphasize an extended role of single atoms as microenvironment regulators, beyond their conventional functions in electronic modulation and adsorption optimization.[23] During the reaction, these sites not only regulate water adsorption and dissociation but also dynamically generate Brønsted acid species (M–O–H*) *in situ*.[24] The formation of these Brønsted acid sites plays a crucial role in modulating the local proton concentration near the Ru active sites.[25] By introducing an appropriate density of such acid sites, the proton concentration in the vicinity of the catalytic centers can be effectively increased, thereby alleviating proton deficiency under alkaline HER conditions.[26] As a result, a localized proton-rich, acid-like interfacial microenvironment is established within the overall alkaline medium, which facilitates more efficient hydrogen evolution.[27] Moreover, compared with Pt, Ru is significantly less expensive while still exhibiting high intrinsic HER activity. Additionally, the rational design and modification of Ru-based materials not only enhance catalytic performance but also offer considerable economic advantages.[28,29]

Here, this study begins with theoretical calculations, investigating the potential impact of introducing Mo, W, and Cr single-atom cocatalysts with oxygen coordination on the HER performance of carbon-supported Ru nanoparticles. Calculations revealed that Mo single-atom cocatalysts could significantly optimize the electronic structure and ΔG_{H^*} of adjacent Ru sites, providing clear theoretical guidance for material synthesis. Subsequently, we synthesized carbon nanotube (CNT)-supported highly dispersed W/Mo/Cr single atoms and Ru nanoparticles (W/Mo/Cr–Ru@CNT) *via* a top-down approach. The Ru particles synergized with W/Mo/Cr single-atom cocatalysts all exhibited superior alkaline HER performance compared to the Ru@CNT material without cocatalysts. Among them, the Ru nanoparticle material regulated by the Mo single-atom cocatalyst showed overpotentials as low as 0 mV and 50.24 mV at current densities of 10 mA cm^{-2} and 100 mA cm^{-2} for alkaline HER, respectively, with a Tafel slope of only 25.34 mV dec^{-1}, and could operate stably for over 200 h. Its performance was significantly better than that of Ru nanoparticle materials regulated by W or Cr single-atom cocatalysts. Combined with analysis using various spectroscopic characterization techniques, we found that the regulation of alkaline HER performance by this type of single-atom cocatalyst extends beyond electronic modulation and hydrogen adsorption energy regulation of the active sites. The introduction of Mo single atoms leads to the formation of stronger Brønsted acidity, which can better regulate protons to meet the demands of neighboring Ru sites and create a proton-enriched acid-like interfacial microenvironment on the catalyst surface. This work expands the application concepts of single-atom cocatalysts and provides a novel perspective for designing efficient single-atom catalysts for alkaline water electrolysis.

Results and discussion

Theoretical prediction and catalyst design

To test our hypothesis that a HER-inactive single atom can serve as an effective cocatalyst, we first evaluated the electronic and adsorption modulation effects of M (M = Mo, W, Cr) single atoms on adjacent Ru clusters. As shown in the computational models in Fig. 1a and S1, M single atoms are anchored on the carbon surface in an M-C_2O_2 configuration, with a Ru_{13} cluster introduced nearby to simulate a Ru nanoparticle. For comparison, we calculated the carbon-supported Ru_{13} cluster (Fig. 1b). First, Bader charge analysis was used to compare the electron distribution of Ru sites adjacent to different M modifications. The Bader charges of the Ru atom connected to the M site (Ru(8)) showed distinct changes (Fig. S2), with the Cr-modified Ru site having the lowest charge (+0.27*e*), while the Ru(8) atom adjacent to W had a Bader charge of +0.37*e* (Fig. 1c). Further comparing the ΔG_{H^*} at these Ru sites, the calculated adsorption energy for the Ru site on the Ru nanoparticle was −0.34 eV (Fig. 1d). After introducing M single atoms, the ΔG_{H^*} of the adjacent Ru sites was significantly optimized, with the degree of

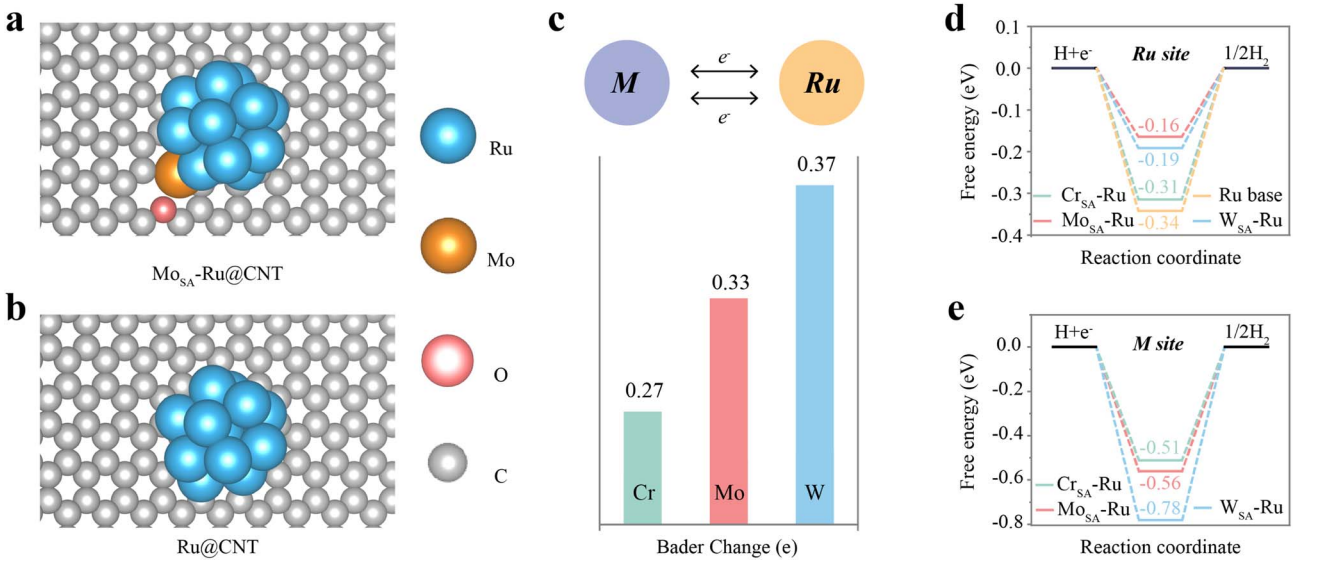

Fig. 1 DFT models and electronic structure modulation analysis of single-atom cocatalyst-modified Ru nanoparticles. (a) Structural model of Mo–Ru@CNT. (b) Structural model of Ru@CNT. (c) Bader charge distribution of Ru(8) atoms adjacent to different M single atoms (M = Mo, W, Cr). (d) Hydrogen adsorption free energy (ΔG_{H*}) of Ru sites with and without single-atom cocatalysts. (e) ΔG_{H*} of single-atom M sites.

optimization following the order: Mo–Ru > W–Ru > Cr–Ru. The Ru site in the Mo–Ru model had the lowest adsorption energy (−0.16 eV). We also calculated the ΔG_{H*} of the M sites (Fig. 1e). All three single-atom sites exhibited non-ideal ΔG_{H*}, indicating that the M sites are less favorable for the HER and primarily serve the auxiliary role of regulating the electronic structure and ΔG_{H*} in this model. Based on the calculation results of these three theoretical models, the Mo single atom is likely the best catalytic promoter among the three elements for optimizing the Ru electronic structure and enhancing the intrinsic HER activity of Ru particles. Therefore, we selected the Mo system for subsequent precise material synthesis and characterization to verify the guiding role of theoretical calculations.

Synthesis and structural characterization of the Mo–Ru@CNT catalyst

We synthesized a carbon nanotube catalyst co-loaded with Mo single atoms and Ru nanoparticles (Mo–Ru@CNT) using a stir-anneal-etch method. The synthesis schematic is shown in Fig. 2a. W–Ru@CNT, Cr–Ru@CNT, and Ru@CNT control samples were prepared using the same strategy. First, the MoO_x–Ru particle precursor was synthesized *via* stirring. Subsequent prolonged etching in acidic and alkaline environments removed the MoO_x particles, leaving only the Mo single atoms stably bound to the substrate. Due to the small particle size of Ru and Mo species, scanning electron microscopy (SEM) mainly showed the morphology of the carbon nanotubes (Fig. 2b). Further transmission electron microscopy (TEM) observations showed the morphology of individual CNTs with obvious particles distributed on the surface (Fig. 2c). High-resolution high-angle annular dark-field scanning transmission electron microscopy (HAADF-STEM) images (Fig. 2d) provided clearer structural information, clearly showing isolated, bright spots distributed across the CNT carrier and surrounding dimmer single bright spots (marked with red circles), corresponding to the structural model in the inset. STEM elemental mapping indicated that the particles were mainly Ru nanoparticles with the Mo element uniformly distributed (Fig. 2e). The contents of Ru and Mo were determined by inductively coupled plasma optical emission spectrometry (ICP-OES), and the results are presented in Table S1.

X-ray absorption fine structure (XAFS) spectroscopy was used to further analyze the local coordination environment of Mo and Ru. The Mo K-edge X-ray absorption near-edge structure (XANES) spectrum (Fig. 2f) shows its absorption edge position lying between that of Mo foil and MoO_3, indicating that the valence state of Mo in Mo–Ru@CNT is between 0 and +6. The corresponding Fourier transform extended X-ray absorption fine structure (FT-EXAFS) spectrum (Fig. 2g) exhibits a main peak at ~1.5 Å, attributed to Mo–O/C coordination, while no peaks corresponding to Mo–Mo metallic bonds at ~2.2 Å and ~3.0 Å are observed, confirming the existence of Mo in single-atom form. The corresponding *k*-space fitting spectra and quantitative EXAFS fitting parameters further confirm the coexistence of Mo–C and Mo–O coordination environments in Mo–Ru@CNT (Fig S3 and Table S2), further supporting the atomic dispersion of Mo species. For Ru, its K-edge XANES spectrum (Fig. 2h) is similar to that of Ru foil, indicating that Ru exists primarily in the metallic state. The FT-EXAFS spectrum of Ru (Fig. 2i) shows significant Ru–O and Ru–Ru coordination peaks at ~1.5 Å and ~2.3 Å, respectively, confirming the presence of Ru nanoparticles. Wavelet transform analysis (Fig. S4) further supports these conclusions. These results are consistent with electron microscopy observations, confirming the successful synthesis of the Mo–Ru@CNT catalyst with Mo single atoms cooperating with Ru particles. Furthermore, to directly probe the electronic structure change of Ru, we performed high-resolution X-ray photoelectron spectroscopy (XPS)

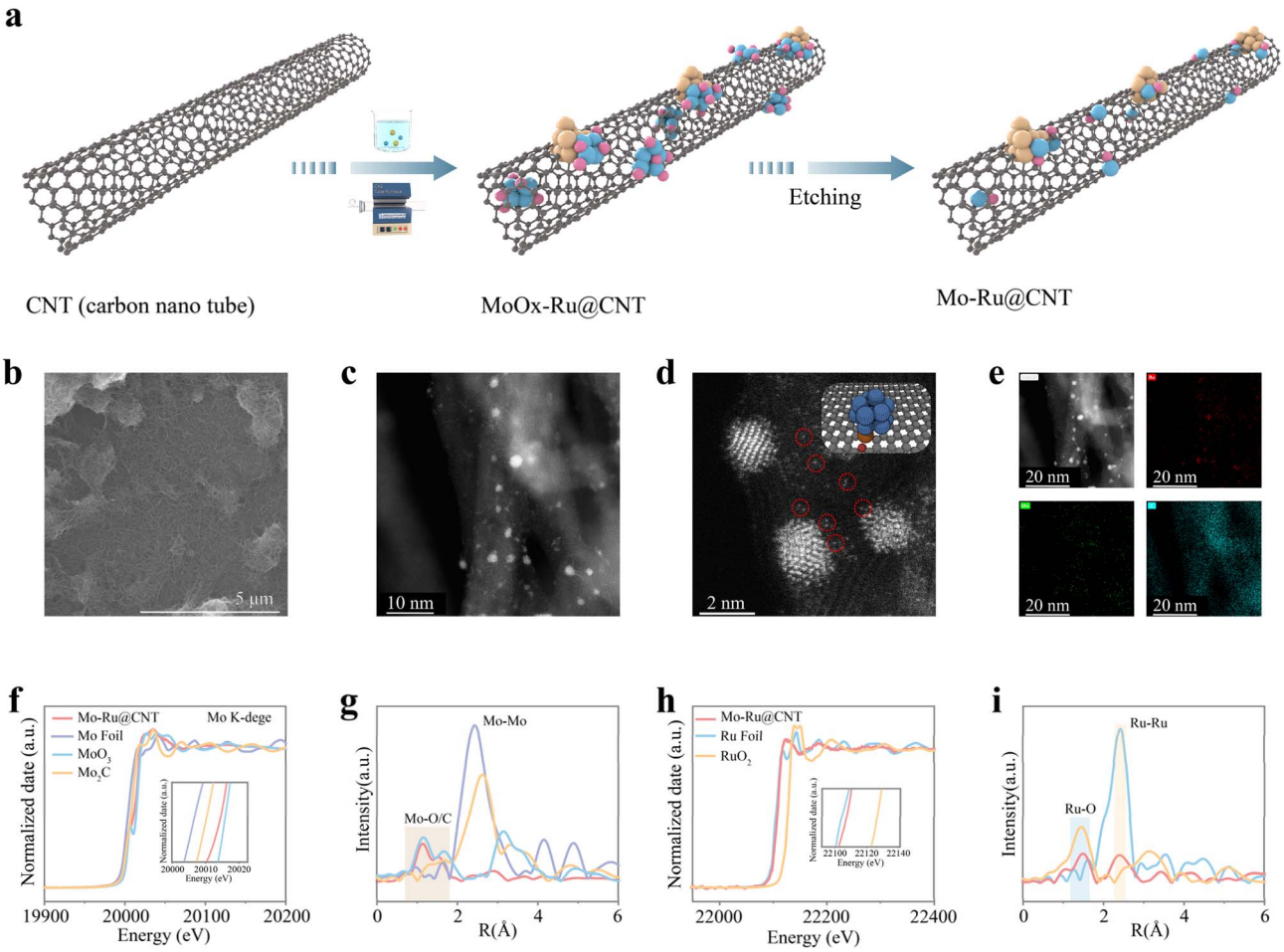

Fig. 2 Structural characterization of the Mo–Ru@CNT catalyst. (a) Schematic illustration of the synthesis process. (b and c) SEM and TEM images showing CNT morphology and nanoparticle distribution. (d) HAADF-STEM image revealing isolated Mo single atoms and Ru nanoparticles. (e) Elemental mapping of Ru and Mo. (f and g) Mo K-edge XANES and FT-EXAFS spectra confirming single-atom Mo coordination. (h and i) Ru K-edge XANES and FT-EXAFS spectra confirming metallic Ru nanoparticles.

measurements in the Ru 3d region, carefully deconvoluting the overlapping C 1s signal (Fig. S5 and Table S3). The binding energy (BE) of metallic Ru $3d_{5/2}$ for both metallic and oxidized Ru species decreases in the order: Ru@CNT > W–Ru@CNT > Mo–Ru@CNT > Cr–Ru@CNT. Compared with Ru@CNT, the BE of Ru in M–Ru@CNT (M = Mo, W, Cr) is negatively shifted, indicating increased electron density on Ru due to electron transfer from the single-atom cocatalysts. The largest BE downshift is observed for Cr–Ru@CNT, followed by Mo–Ru@CNT and then W–Ru@CNT, suggesting that the extent of electron transfer follows Cr > Mo > W. This trend is fully consistent with our Bader charge analysis and confirms that the introduction of single-atom cocatalysts effectively modulates the electronic structure of adjacent Ru nanoparticles.

Electrochemical hydrogen evolution performance evaluation

The alkaline HER performance of Mo–Ru@CNT and other comparison samples was evaluated in 1.0 M KOH solution. Linear sweep voltammetry (LSV) curves are shown in Fig. 3a. Mo–Ru@CNT exhibited the highest activity, with an overpotential close to 0 mV at 10 mA cm^{-2} and only 50.24 mV at 100 mA cm^{-2}. Meanwhile, Cr–Ru@CNT (η_{10} = 0 mV, η_{100} = 58.24 mV) and W–Ru@CNT (η_{10} = 19.29 mV, η_{100} = 153.43 mV) also performed significantly better than the unmodified Ru@CNT (η_{10} = 30.42 mV, η_{100} = 242.55 mV). For comparison, the alkaline HER performance of Mo@CNT containing only atomically dispersed Mo sites was also evaluated. Mo@CNT exhibited extremely poor HER activity, requiring substantially higher overpotentials to reach the same current densities (Fig. S6). This result confirms that isolated Mo single atoms do not serve as effective HER active centers and instead primarily function as auxiliary cocatalytic regulators in the Mo–Ru@CNT system. For each sample, 95% iR compensation was applied for each LSV measurement. The catalysts were scanned independently three times. The average overpotential and its standard deviation at representative current densities of 10, 50, 100, and 200 mA cm^{-2} are summarized in Table S4 and are shown in the inset of Fig. S7. The smaller error bars indicate good repeatability of the electrochemical measurements. Additionally, Fig. S8 and S9 provide the iR-compensated and uncompensated polarization curves of representative samples, further confirming that the performance of Mo–Ru@CNT sample is reliable. Although the overpotential of

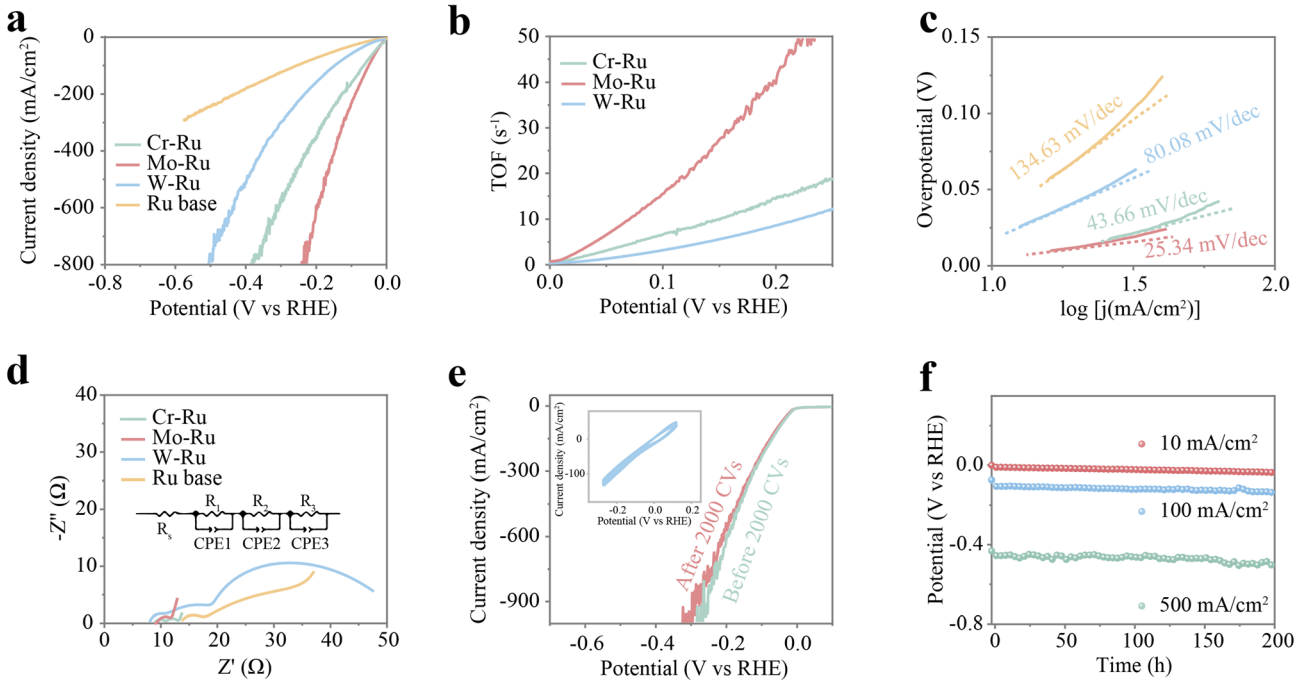

Fig. 3 Electrochemical HER performance of Mo–Ru@CNT and comparison catalysts in 1.0 M KOH. (a) LSV polarization curves. (b) TOF. (c) Tafel plots. (d) EIS plots, with an inset showing the fitted equivalent circuit model. (e and f) Stability evaluation including cyclic voltammetry durability and long-term chronoamperometric tests.

Cr–Ru@CNT at low potential was similar to that of Mo–Ru@CNT, this is attributed to the larger electrochemically active surface area of the Cr–Ru@CNT material (Fig. S10), not an improvement in intrinsic activity. Further evaluation of intrinsic activity *via* turnover frequency (TOF) was conducted, using Ru as the active center and calculating TOF based on Ru content measured by ICP. As shown in Fig. 3b, the TOF values for different samples indicate that at an overpotential of 100 mV, the TOF value for Mo–Ru@CNT reached 15.49 s^{-1}, which is 2.3 times higher than that of Cr–Ru@CNT and 4.9 times higher than that of W–Ru@CNT. In addition, ECSA-normalized HER polarization curves (Fig. S11) further confirm the enhanced intrinsic activity of Mo–Ru@CNT. Corresponding Tafel slope analysis (Fig. 3c) shows that Mo–Ru@CNT has the smallest slope (25.34 mV dec^{-1}), lower than those of Cr–Ru@CNT (43.66 mV dec^{-1}), W–Ru@CNT (80.08 mV dec^{-1}), and Ru@CNT (134.63 mV dec^{-1}), indicating its fastest reaction kinetics. The addition of M cocatalysts breaks the rate-limiting Volmer step for Ru particles in alkaline HER and gradually shifts the reaction process towards the Volmer–Tafel pathway. For the charge transfer resistance during the reaction, electrochemical impedance spectroscopy (EIS, Fig. 3d) was used for further evaluation. The Nyquist plots were fitted using an equivalent circuit model (inset of Fig. 3d), and the fitted parameters (Table S5) are summarized accordingly. The comparison confirmed that Mo–Ru@CNT has the smallest charge transfer resistance (R_2), implying faster interfacial charge transfer. To evaluate the stability of the material (Fig. 4e and f), the Mo–Ru@CNT catalyst showed negligible performance degradation after 2000 cycles of cyclic voltammetry testing and could operate stably for nearly 200 hours at current densities of 10, 100, and 500 mA cm^{-2}, with decay rates of 116.9, 133.5, and 210.0 μV h^{-1}, respectively, demonstrating decent stability.[30,31] The HER performance of Mo–Ru@CNT was further compared with recently reported state-of-the-art alkaline HER catalysts (Fig. S12 and Table S6), demonstrating its competitive activity and stability among recently reported alkaline HER catalysts.

Probing the reaction mechanism

To verify the enhancement effect of single-atom cocatalysts on the alkaline HER performance of Ru particles, we compared the surface acidity of three samples after electrochemical reaction using pyridine infrared spectroscopy (Fig. 4a and b). The results show that the introduction of M single atoms significantly increased the solid acid content on the catalyst surface. Notably, after introducing Mo single atoms, the content of surface Brønsted acid was more significantly enhanced, and the Lewis acid intensity was also the highest, with the corresponding B/L acid ratio being the largest (Table S7). To further quantitatively evaluate the acid-site properties, NH_3-TPD measurements were performed on Mo–Ru@CNT, Cr–Ru@CNT, and W–Ru@CNT (Fig. S13). Compared with Cr–Ru@CNT and W–Ru@CNT, Mo–Ru@CNT exhibits a more pronounced desorption peak at higher temperature, indicating stronger acid-site strength.[32] This result is consistent with the pyridine-IR analysis, confirming that the introduction of Mo single atoms leads to enhanced Brønsted acidity. To verify that the enhanced surface acidity originates from atomically dispersed Mo sites rather than from Ru nanoparticles or non-single-atom Mo species, we conducted control experiments on post-reaction Ru@CNT (without Mo) and unetched MoO_x–Ru@CNT (containing MoO_x species before

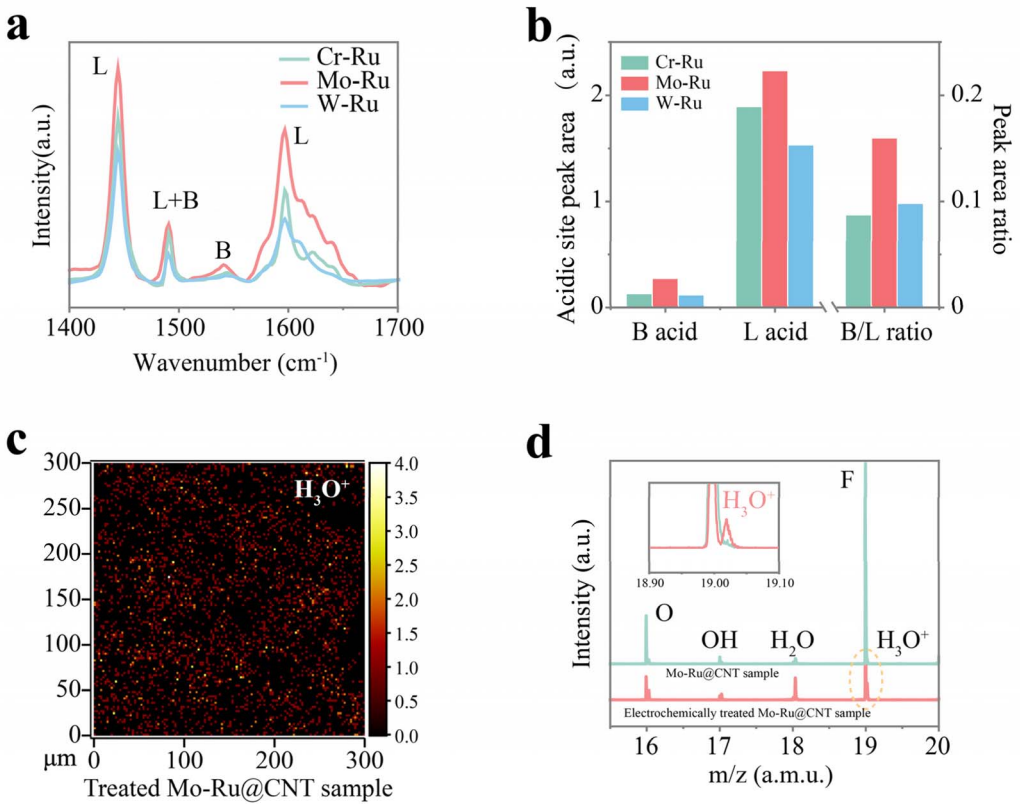

Fig. 4 Experimental investigation of interfacial acidity and proton regulation. (a) Pyridine-IR spectra of Mo–Ru@CNT, Cr–Ru@CNT, and W–Ru@CNT after electrochemical treatment. (b) Quantitative analysis of Brønsted and Lewis acid sites. (c) TOF-SIMS mapping of hydronium ion (H_3O^+) distribution on the treated Mo–Ru@CNT surface. (d) TOF-SIMS plots.

acid–alkali etching). Py-IR results (Fig. S14 and Table S7) showed that Mo–Ru@CNT had the highest Brønsted and Lewis acid contents, followed by MoO_x–Ru@CNT and then Ru@CNT. This indicates that Ru nanoparticles alone contribute limited surface acidity, and non-single-atom MoO_x species cannot account for the pronounced acidity observed in

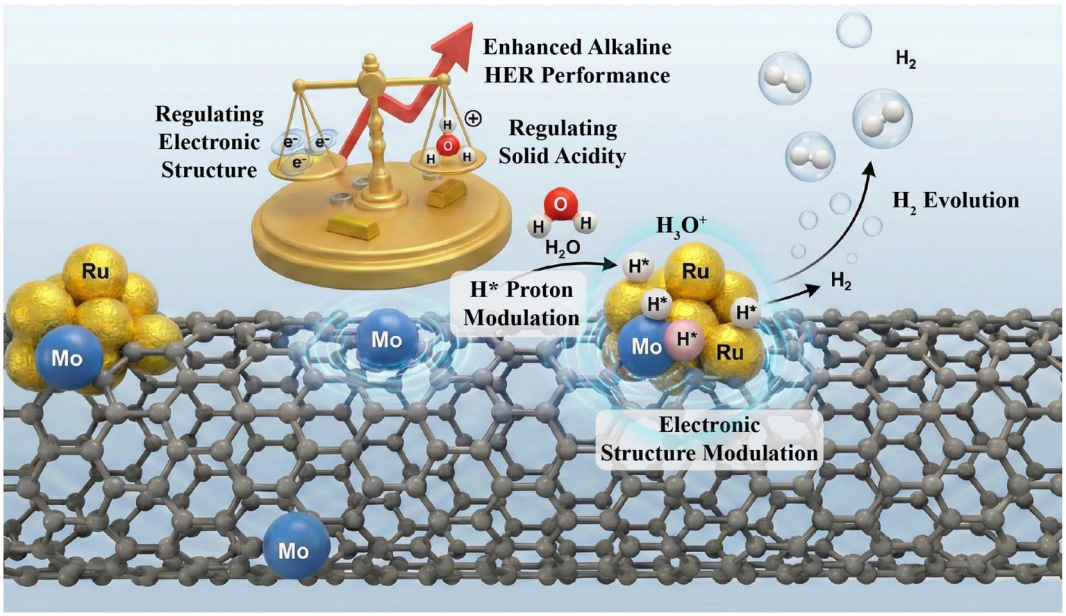

Scheme 1 Schematic illustration of the single-atom cocatalyst-assisted alkaline HER mechanism, showing electronic structure modulation, Brønsted acid formation, proton regulation, and synergistic hydrogen evolution on Ru nanoparticles.

Mo–Ru@CNT. Therefore, the markedly enhanced solid acidity of Mo–Ru@CNT is mainly attributed to the atomically dispersed Mo cocatalyst sites. Furthermore, time-of-flight secondary ion mass spectrometry (TOF-SIMS) directly detected the formation of hydronium ions on the surface after the electrochemical reaction. Compared to the surface of Mo–Ru@CNT without electrochemical treatment, the significant presence of hydronium ions is attributed to proton regulation by the Brønsted acid. To experimentally verify the above mechanism, we performed TOF-SIMS analysis on the surface of the Mo–Ru@CNT electrode after the HER reaction. As shown in Fig. 4c and d, a significant H_3O^+ fragment signal was detected on the Mo–Ru@CNT electrode surface, with an intensity much higher than that of the unreacted pristine sample and the post-reaction pure Ru@CNT electrode (Fig. S15). This proves that under working potential, the Mo single-atom cocatalyst sites can induce the enrichment of H_3O^+ at the electrode/electrolyte interface, thereby breaking the proton-deficient dilemma at the alkaline HER interface and enhancing alkaline HER performance. Furthermore, quasi-*operando* TOF-SIMS measurements were performed to probe the dynamic evolution of proton-related interfacial species during alkaline HER. As shown in Fig. S16, the results show that the H_3O^+-related signal is weak on the pristine electrode and after simple KOH immersion, but gradually increases as the applied cathodic potential enters the HER working region. At higher HER overpotentials, the signal becomes significantly stronger and more uniformly distributed across the catalyst surface. The corresponding mass spectra also exhibit a consistent enhancement of the H_3O^+-related fragment intensity with increasing HER polarization. Importantly, this evolution trend closely correlates with the simultaneously observed increase of Mo–OH fragments under HER conditions (Fig. S17), indicating that the dynamically generated hydroxylated/protonated Mo species are closely associated with the enrichment of protonated interfacial species. A control TOF-SIMS measurement on Ru@CNT under identical conditions shows a weak H_3O^+-related signal (Fig. S18). Combined with the *in situ* TOF-SIMS analysis, this finding confirms that the enhanced signal on Mo–Ru@CNT is not due to surface hydration but originates from Mo-induced interfacial processes.

Therefore, based on the above theoretical calculations and experimental data analysis, we propose an alkaline HER mechanism based on single-atom cocatalysts, mainly demonstrating the electronic and proton regulation effects of the Mo single-atom cocatalyst on active sites during alkaline HER (Scheme 1). First, the introduction of Mo sites modulates the electronic structure of Ru sites, thereby enhancing the intrinsic HER activity of Ru sites. Furthermore, as a cocatalyst, the single-atom site can *in situ* form Brønsted acid sites during the reaction. These sites have the ability to store and donate protons, thereby regulating the proton environment of neighboring active sites. Additionally, due to the strongest Brønsted acidity introduced by Mo single atoms, protons further enrich to form a localized acidic environment. This provides abundant protons for the Ru active sites, greatly enhancing the HER performance of alkaline water electrolysis.

Conclusions

This study establishes single-atom cocatalysts as a new functional category for engineering reaction microenvironments in alkaline water electrolysis. Through a theoretical calculation-driven synthesis strategy, this work reveals the critical role of Brønsted acid-characteristic single-atom cocatalysts in regulating hydrogen evolution under alkaline conditions. Guided by theoretical predictions, Mo single-atom cocatalyst-modified Ru nanoparticles were selected as a representative model catalyst. The resulting catalyst exhibited outstanding alkaline HER performance, delivering overpotentials as low as 0 and 50.24 mV at current densities of 10 and 100 mA cm^{-2}, respectively, together with a low Tafel slope of 25.34 mV dec^{-1}, a high turnover frequency of 15.49 s^{-1} at an overpotential of 100 mV, and stable operation for 200 h. Combined theoretical calculations and multi-scale spectroscopic characterization demonstrate that the introduction of Mo single-atom cocatalysts significantly modulates the catalytic behavior of adjacent Ru sites. Specifically, the cocatalyst not only optimizes the electronic structure and intrinsic hydrogen adsorption energetics of Ru active centers but also dynamically generates Brønsted acid sites during operation. These acid sites regulate the local proton environment, facilitate proton transfer, and establish a proton-enriched acid-like interfacial microenvironment. The successful implementation of single-atom cocatalysts in alkaline water electrolysis expands the functional scope of single-atom materials from conventional electronic/adsorption regulators toward dynamic interfacial microenvironment regulators for complex electrocatalytic reactions.

Author contributions

G. Yang: conceptualization, methodology, investigation, formal analysis, writing—original draft. M. Yang: methodology (DFT calculations), investigation. Z. Meng: investigation (assistance with catalyst synthesis), formal analysis, supervision (theoretical insights). Y. Cui: supervision, writing—review and editing, funding acquisition. Y. Kang: supervision, project administration, writing—review and editing.

Conflicts of interest

The authors declare no conflict of interests.

Data availability

The data are available from the corresponding author on reasonable request.

Supplementary information (SI): experimental details, additional characterization data (including, XPS, WT-EXAFS, NH_3-TPD, Py-IR and TOF-SIMS images), electro chemical performance plots, tables summarizing catalytic metrics, and details of the DFT calculation models. See DOI: https://doi.org/10.1039/d6sc01375a.

Acknowledgements

We would like to acknowledge the support from the Natural Science Foundation of Jiangsu Province (BK20241821) and the National Key R&D Program of China (No. 2022YFA1503802). The authors are grateful for the technical support of Nano-X from Suzhou Institute of Nano-Tech and Nano-Bionics, Chinese Academy of Sciences (SINANO).

References

1 Y. Wan, R. Li, J. Su, W. Yi, Y. Li, H. Chu, Z. Shen, S. Gao, X. Hai, R. Zhong and R. Zou, *Adv. Mater.*, 2025, **37**, 2504518.
2 B. Jiang, J. Zhu, Z. Xia, J. Lyu, X. Li, L. Zheng, C. Chen, S. Chaemchuen, T. Bu, F. Verpoort, S. Mu, J. Wu, J. Wang and Z. Kou, *Adv. Mater.*, 2024, **36**, 2310699.
3 B. Jiang, H. Zhang, R. Pan, M. Ji, L. Zhu, G. Zhang, J. Liu, H. Shi, H. Huang, S. Wan, K. Yin and L. Sun, *Angew. Chem., Int. Ed.*, 2025, **64**, e202500474.
4 B. Qiao, A. Wang, X. Yang, L. F. Allard, Z. Jiang, Y. Cui, J. Liu, J. Li and T. Zhang, *Nat. Chem.*, 2011, **3**, 634.
5 H. Chen, Z. Huang, J. Wang, Y. Zhu, X. Liu, G. Zhang, Q. Li, H. Dai, S. Chen, H. Liu, Z. Wang and J. Zou, *ACS Catal.*, 2026, 2976.
6 Y. Li, S. Niu, P. Liu, R. Pan, H. Zhang, N. Ahmad, Y. Shi, X. Liang, M. Cheng, S. Chen, J. Du, M. Hu, D. Wang, W. Chen and Y. Li, *Angew. Chem., Int. Ed.*, 2024, **63**, e202316755.
7 Z. Jiang, W. Sun, H. Shang, W. Chen, T. Sun, H. Li, J. Dong, J. Zhou, Z. Li, Y. Wang, R. Cao, R. Sarangi, Z. Yang, D. Wang, J. Zhang and Y. Li, *Energy Environ. Sci.*, 2019, **12**, 3508.
8 S. Vallem, M. G. Sibi, R. Patil, V. Goyal, A. Giridhar Babu, Ea. Lohith, K. Keerthi, M. Umer, N. V. V. Jyothi, M. Vandichel, D. I. Stroe, S. Ray, M. Balamurugan, A. Bakandritsos, S. Venkateswarlu, R. V. Jagadeesh and R. Zboril, *Energy Environ. Sci.*, 2025, **18**, 9632.
9 S. Zhang, Y. Song, Y. Liu, Z. Ma, S. Zhan, Z. Wang, L. Zhang, T. Liu and Y. Xie, *ACS Nano*, 2025, **19**, 31690.
10 X. Shi, Z. Wen, Q. Gu, L. Jiao, H.-L. Jiang, H. Lv, H. Wang, J. Ding, M. P. Lyons, A. Chang, Z. Feng, S. Chen, Y. Lin, X. Xu, P. Du, W. Xu, M. Sun, Y. Li, B. Yang, T. Zhang, X. Wu and J. Lu, *Nature*, 2025, **640**, 668.
11 H.-M. Yan, G. Wang, X.-M. Lv, H. Cao, G.-Q. Qin and Y.-G. Wang, *J. Am. Chem. Soc.*, 2025, **147**, 3724.
12 D. Miao, J. Li, J. Ren and Z. Chen, *Adv. Mater.*, 2026, e20491.
13 M. Chatenet, B. G. Pollet, D. R. Dekel, F. Dionigi, J. Deseure, P. Millet, R. D. Braatz, M. Z. Bazant, M. Eikerling, I. Staffell, P. Balcombe, Y. Shao-Horn and H. Schäfer, *Chem. Soc. Rev.*, 2022, **51**, 4583.
14 L. Jiang, X. Chen, L. Jiang, X. Luo, R. Li, Q. Zhou, X. Mu, L. Chen, B. Li, J. Yu and S. Mu, *ACS Catal.*, 2025, **15**, 14380.
15 Z. Yu, Y. Duan, X. Feng, X. Yu, M. Gao and S. Yu, *Adv. Mater.*, 2021, **33**, 2007100.
16 H. Su, W. Liao, S. Mo, H. Wang, Y. Cao, H. Yu and H. Wang, *Adv. Funct. Mater.*, 2025, e18373.
17 M.-X. Li, Y. Ma, B. Xiao, Y.-N. Zhou, W.-L. Yu, X.-J. Zhai, R.-Q. Lv, Y.-M. Chai and B. Dong, *Chem. Eng. J.*, 2023, **470**, 144081.
18 R. Subbaraman, D. Tripkovic, D. Strmcnik, K.-C. Chang, M. Uchimura, A. P. Paulikas, V. Stamenkovic and N. M. Markovic, *Science*, 2011, **334**, 1256.
19 Y. Kang, C. Zhang, H. Li, Y. Li, H. Lei, R. Huang, Y. Han, W. Wei, X. Zhao and Y. Cui, *ACS Catal.*, 2025, **15**, 8768.
20 L. Zeng, Z. Zhao, Q. Huang, C. Zhou, W. Chen, K. Wang, M. Li, F. Lin, H. Luo, Y. Gu, L. Li, S. Zhang, F. Lv, G. Lu, M. Luo and S. Guo, *J. Am. Chem. Soc.*, 2023, **145**, 21432.
21 C. Zhou, J. Shi, Z. Dong, L. Zeng, Y. Chen, Y. Han, L. Li, W. Zhang, Q. Zhang, L. Gu, F. Lv, M. Luo and S. Guo, *Nat. Commun.*, 2024, **15**, 6741.
22 Z. Chen, M. Yang, Y. Li, W. Gong, J. Wang, T. Liu, C. Zhang, S. Hou, G. Yang, H. Li, Y. Jin, C. Zhang, Z. Tian, F. Meng and Y. Cui, *Nat. Commun.*, 2025, **16**, 418.
23 G. Busca, *Phys. Chem. Chem. Phys.*, 1999, **1**, 723.
24 Z. Chen, W. Gong, J. Wang, S. Hou, G. Yang, C. Zhu, X. Fan, Y. Li, R. Gao and Y. Cui, *Nat. Commun.*, 2023, **14**, 5363.
25 S. Hou, Y. Xu, Z. Chen, G. Yang, C. Zhu, X. Fan, X. Weng, J. Wang, L. Wang and Y. Cui, *ACS Catal.*, 2024, **14**, 8238.
26 G. Yang, C. Zhang, Z. Chen, J. Wang, G. Gao, Z. Li, R. Huang and Y. Cui, *ACS Catal.*, 2025, **15**, 2270.
27 H. Tan, B. Tang, Y. Lu, Q. Ji, L. Lv, H. Duan, N. Li, Y. Wang, S. Feng, Z. Li, C. Wang, F. Hu, Z. Sun and W. Yan, *Nat. Commun.*, 2022, **13**, 2024.
28 D. H. Kweon, M. S. Okyay, S.-J. Kim, J.-P. Jeon, H.-J. Noh, N. Park, J. Mahmood and J.-B. Baek, *Nat. Commun.*, 2020, **11**, 1278.
29 C. Wu, T. Wu, Z. Tang, J. Dai, B. Zeng, Y. Xu, G. Chen, W. Luo, C. Yuan and L. Dai, *Nanotechnology*, 2022, **33**, 405401.
30 H. Liu, Q. Yu, J. Liu, H. Chen, Y. Chen, T. Zhang, J. Khan, Y. Dong, X. Kang, L. Liu, H.-M. Cheng and B. Liu, *Natl. Sci. Rev.*, 2025, **12**, nwaf311.
31 X. Kang, F. Yang, Z. Zhang, H. Liu, S. Ge, S. Hu, S. Li, Y. Luo, Q. Yu, Z. Liu, Q. Wang, W. Ren, C. Sun, H.-M. Cheng and B. Liu, *Nat. Commun.*, 2023, **14**, 3607.
32 S. Hou, Z. Chen, M. Yang, X. Hou, G. Yang, C. Zhang, J. Wang, Y. Li and Y. Cui, *ACS Catal.*, 2025, **15**, 16427.